OES | Opto-Electronic Science

Supplementary information

August 2026, Vol. 5, No. 8

Open Access

Physics-informed neural fields enable blind aberration correction for partially coherent quantitative phase imaging

Shun Zhou[1,2,3†], Xingyu Huang[1,2,3†], Linpeng Lu[1,2,3], Habib Ullah[1,2,3], Kaiyu Du[1,2,3], Maciej Trusiak[4], Malgorzata Kujawinska[4], Yuzhen Zhang[3], Yao Fan[1,2,3*], Qian Chen[3,5*], Qinrong Zhang[6*] and Chao Zuo[1,2,3,5*]

[1]Smart Computational Imaging Laboratory (SCILab), School of Electronic and Optical Engineering, Nanjing University of Science and Technology, Nanjing 210094, China; [2]Smart Computational Imaging Research Institute (SCIRI), Nanjing University of Science and Technology, Nanjing 210019, China; [3]Jiangsu Key Laboratory of Visual Sensing & Intelligent Perception, Nanjing University of Science and Technology, Nanjing 210094, China; [4]Institute of Micromechanics and Photonics, Warsaw University of Technology, Warsaw 02-525, Poland; [5]State Key Laboratory of Extreme Environment Optoelectronic Dynamic Measurement Technology and Instrument, Taiyuan 030051, China; [6]Department of Biomedical Engineering, City University of Hong Kong, Hong Kong 999077, China.
[†]These authors contributed equally to this work.
*Correspondence: Y Fan, E-mail: fanyao@njust.edu.cn; Q Chen, E-mail: chenqian@njust.edu.cn; QR Zhang, E-mail: qzhan32@cityu.edu.hk; C Zuo, E-mail: zuochao@njust.edu.cn

This file includes:

Section 1. Derivation of the explicit update formula in USDPC
Section 2. Analysis of loss function composition and parameter selection
Section 3. Analysis of coordinate encoding and MLP depth
Section 4. Robustness analysis of USDPC for reconstructing large-phase samples
Section 5. Numerical characterization of the aberration correction capability of USDPC
Section 6. Numerical evaluation of the noise robustness of USDPC
Section 7. Analysis of the subregion partitioning and stitching strategy
Section 8. Evaluation metrics for assessing the image quality in quantitative phase imaging
Section 9. Quantitative phase imaging of unstained biological tissue section
Section 10. Validation of USDPC under different objective numerical apertures
Section 11. Analysis of the data requirement for stable USDPC reconstruction

Supplementary information for this paper is available at https://doi.org/10.29026/oes.2026.260019

Section 1. Derivation of the explicit update formula in USDPC

Although the neural-field framework allows the use of automatic differentiation provided by PyTorch to implicitly compute the gradients of the loss function with respect to the trainable parameters via a computational graph[S1], we derived here the explicit update formulas to clarify the optimization process[S2]. The parameter propagation processes of these two multilayer perceptrons (MLPs) can be expressed as

$$\boldsymbol{f}_{i+1}^{\mathrm{o}} = \sigma_i^{\mathrm{o}}(\boldsymbol{g}_i^{\mathrm{o}}) = \sigma_i^{\mathrm{o}}\left(\boldsymbol{W}_i^{\mathrm{o}}\boldsymbol{f}_i^{\mathrm{o}}\right), \tag{S1}$$

here $\boldsymbol{W}_i^{\mathrm{o}}$, $\boldsymbol{f}_i^{\mathrm{o}}$, σ_i^{o} and $\boldsymbol{f}_{i+1}^{\mathrm{o}}$denote the weight matrix, input, activation function, and output of the i^{th} layer of object MLP, respectively. The sample's phase and absorption and optical aberration can be related to the network output through the following equation:

$$\begin{pmatrix}\phi(\boldsymbol{r})\\ a(\boldsymbol{r})\end{pmatrix} = \boldsymbol{M}\begin{pmatrix}\boldsymbol{f}_{N_{\mathrm{o}}+1}^{\mathrm{o},\phi}\\ \boldsymbol{f}_{N_{\mathrm{o}}+1}^{\mathrm{o},a}\end{pmatrix}, \tag{S2}$$

$$\begin{cases}\boldsymbol{k} = \boldsymbol{T}\sigma^{\mathrm{s}}(\boldsymbol{g}^{\mathrm{s}}) = \boldsymbol{T}\sigma^{\mathrm{s}}(\boldsymbol{W}^{\mathrm{s}}\boldsymbol{f}^{\mathrm{s}})\\ P(\boldsymbol{u}) = \mathrm{circ}\left(\dfrac{\boldsymbol{u}}{\mathrm{NA}/\lambda}\right)\mathrm{e}^{\mathrm{j}\sum_m^M \boldsymbol{k}(m)Z_m(\boldsymbol{u})}\end{cases}, \tag{S3}$$

where $\boldsymbol{f}_{N_{\mathrm{o}}+1}^{\mathrm{o},\phi}$ and $\boldsymbol{f}_{N_{\mathrm{o}}+1}^{\mathrm{o},a}$ represent two output channels of the last layer of object MLP, $\boldsymbol{W}_{N_{\mathrm{o}}}^{\mathrm{o}}$. $\boldsymbol{M}$ is the transformation matrix used to map these outputs to the corresponding physical parameters. $\boldsymbol{W}^{\mathrm{s}}$, $\boldsymbol{f}^{\mathrm{s}}$, σ^{s}, and $\boldsymbol{k}$ is the weight matrix, input, activation function, and output (Zernike coefficient matrix). $\boldsymbol{T}$ represents the transformation matrix. $Z_m(\boldsymbol{u})$ is the Zernike polynomial corresponding to the m^{th} mode, $\boldsymbol{k}(m)$ represents its associated coefficient, and $\mathrm{circ}(\boldsymbol{u}/(\mathrm{NA}/\lambda))$ represents an ideal low-pass filter with a cutoff frequency of NA/λ.

The training process updates network parameters via gradient descent by minimizing a hybrid loss function that includes mean squared error (MSE), structural similarity index (SSIM), and total variation (TV) regularization term. The hybrid loss function is defined as

$$\mathscr{L} = \frac{1}{4}\sum_{i=1}^{4}\left\{\left\|\boldsymbol{F}(a,\phi,P,S_i) - I_i\right\|_{\ell_2}^2 + \eta\left(1 - \mathrm{SSIM}\left(\boldsymbol{F}(a,\phi,P,S_i), I_i\right)\right)\right\} + \tau\mathscr{R}_{\mathrm{tv}}(a,\phi), \tag{S4}$$

where $\boldsymbol{F}(\cdot)$ is the forward operator computed via Eq. (1) in the main text. The SSIM-based data fidelity term is defined as

$$\mathrm{SSIM}(\boldsymbol{F}(a,\phi,P,S_i), I_i) = \frac{(2\mu_{\mathscr{F}}\mu_I + C_1)(2o_{\mathscr{F}I} + C_2)}{(\mu_{\mathscr{F}}^2 + \mu_I^2 + C_1)(o_{\mathscr{F}}^2 + o_I^2 + C_2)}, \tag{S5}$$

here, $\mu_{\mathscr{F}}$ and μ_I are the mean values of the predicted intensity $\boldsymbol{F}(a,\phi,P,S_i)$ and the measured intensity I_i, respectively. $o_{\mathscr{F}}^2$ and o_I^2 represent the variances of the functions $\boldsymbol{F}(a,\phi,P,S_i)$ and I_i, respectively, and $o_{\mathscr{F}I}$ is the covariance between $\boldsymbol{F}(a,\phi,P,S_i)$ and I_i. The constants C_1 and C_2 are included to ensure numerical stability and are typically set to small positive values. $\mathscr{R}_{\mathrm{TV}}$ denotes the TV regularization term, defined as

$$\mathscr{R}_{TV} = \nabla\phi(\boldsymbol{r}) + \nabla a(\boldsymbol{r}), \tag{S6}$$

where $\nabla\phi(\boldsymbol{r})$ and $\nabla a(\boldsymbol{r})$ denote the spatial gradients of the phase and absorption distributions, with the objective of minimizing these gradients and promoting spatial smoothness.

According to the chain rule, the gradient of the loss function with respect to the $\boldsymbol{f}_i$ and $\boldsymbol{W}_i$ of i^{th} layer can be written as

$$\begin{aligned}\frac{\partial\mathscr{L}}{\partial\boldsymbol{f}_i} &= \frac{\partial\mathscr{L}}{\partial\boldsymbol{f}_{i+1}}\frac{\partial\boldsymbol{f}_{i+1}}{\partial\boldsymbol{g}_i}\frac{\partial\boldsymbol{g}_i}{\partial\boldsymbol{f}_i} = \frac{\partial\mathscr{L}}{\partial\boldsymbol{f}_{i+1}}\sigma'\left(\boldsymbol{f}_i\boldsymbol{W}_i\right)\boldsymbol{W}_i^{\mathrm{T}}\\ \frac{\partial\mathscr{L}}{\partial\boldsymbol{W}_i} &= \frac{\partial\mathscr{L}}{\partial\boldsymbol{f}_{i+1}}\frac{\partial\boldsymbol{f}_{i+1}}{\partial\boldsymbol{g}_i}\frac{\partial\boldsymbol{g}_i}{\partial\boldsymbol{W}_i} = \boldsymbol{f}_i^{\mathrm{T}}\frac{\partial\mathscr{L}}{\partial\boldsymbol{f}_{i+1}}\sigma'\left(\boldsymbol{f}_i\boldsymbol{W}_i\right)\end{aligned}. \tag{S7}$$

The gradients of the loss function $\mathscr{L}$ with respect to the MLP outputs can be related to the gradients of the physical quantities $(\phi,\ a,\ \boldsymbol{k})$ via the following relationship:

$$\begin{aligned}\begin{pmatrix}\dfrac{\partial \mathscr{L}}{\partial \boldsymbol{f}^{\mathrm{o},\phi}_{N_\mathrm{o}+1}}\\ \dfrac{\partial \mathscr{L}}{\partial \boldsymbol{f}^{\mathrm{o},a}_{N_\mathrm{o}+1}}\end{pmatrix} &= \boldsymbol{M}^{\mathrm{T}}\begin{pmatrix}\dfrac{\partial \mathscr{L}}{\partial \phi(\boldsymbol{r})}\\ \dfrac{\partial \mathscr{L}}{\partial a(\boldsymbol{r})}\end{pmatrix}\\ \frac{\partial \mathscr{L}}{\partial \boldsymbol{f}^{\mathrm{s}}_{N_\mathrm{s}+1}} &= \boldsymbol{T}^{\mathrm{T}}\frac{\partial \mathscr{L}}{\partial \boldsymbol{k}}\end{aligned}, \tag{S8}$$

here, $\dfrac{\partial \mathscr{L}}{\partial \phi(\boldsymbol{r})}$ and $\dfrac{\partial \mathscr{L}}{\partial a(\boldsymbol{r})}$ denote the gradients of the loss function with respect to the reconstructed phase and absorption, respectively. $\boldsymbol{M}^{\mathrm{T}}$ represents the transposed transformation matrix. $\dfrac{\partial \mathscr{L}}{\partial \boldsymbol{f}^{\mathrm{o},\phi}_{N_\mathrm{o}+1}}$ and $\dfrac{\partial \mathscr{L}}{\partial \boldsymbol{f}^{\mathrm{o},a}_{N_\mathrm{o}+1}}$ correspond to the gradients of the loss function with respect to the outputs of the object reconstruction network. $\dfrac{\partial \mathscr{L}}{\partial \boldsymbol{k}}$ denotes the gradient of the loss function with respect to the Zernike coefficients, while $\dfrac{\partial \mathscr{L}}{\partial \boldsymbol{f}^{\mathrm{s}}_{N_\mathrm{s}+1}}$ represents the gradient of the loss function with respect to the output of the optical aberration network. $\boldsymbol{T}^{\mathrm{T}}$ is the transpose of the corresponding linear transformation matrix. N_o and N_s denote the total number of layers in the object reconstruction and optical aberration MLPs, respectively. Accordingly, the network parameters are iteratively updated during the training process through gradient descent as

$$\begin{cases}\boldsymbol{W}^{\mathrm{o}}_i = \boldsymbol{W}^{\mathrm{o}}_i - \alpha^{\mathrm{o}}\dfrac{\partial \mathscr{L}}{\partial \boldsymbol{W}^{\mathrm{o}}_i}\\ \boldsymbol{W}^{\mathrm{s}}_i = \boldsymbol{W}^{\mathrm{s}}_i - \alpha^{\mathrm{s}}\dfrac{\partial \mathscr{L}}{\partial \boldsymbol{W}^{\mathrm{s}}_i}\end{cases}, \tag{S9}$$

where α^{o} and α^{s} correspond to the update step size of two MLPs. $\dfrac{\partial \mathscr{L}}{\partial \boldsymbol{W}^{\mathrm{o}}_i}$ and $\dfrac{\partial \mathscr{L}}{\partial \boldsymbol{W}^{\mathrm{s}}_i}$ are expressed as

$$\begin{cases}\begin{cases}\dfrac{\partial \mathscr{L}}{\partial \boldsymbol{f}^{\mathrm{o}}_i} = \dfrac{\partial \mathscr{L}}{\partial \boldsymbol{f}^{\mathrm{o}}_{i+1}}\dfrac{\partial \boldsymbol{f}^{\mathrm{o}}_{i+1}}{\partial \boldsymbol{g}^{\mathrm{o}}_i}\dfrac{\partial \boldsymbol{g}^{\mathrm{o}}_i}{\partial \boldsymbol{f}^{\mathrm{o}}_i} = \dfrac{\partial \mathscr{L}}{\partial \boldsymbol{f}^{\mathrm{o}}_{i+1}}\sigma'\left(\boldsymbol{f}^{\mathrm{o}}_i\boldsymbol{W}^{\mathrm{o}}_i\right)\left(\boldsymbol{W}^{\mathrm{o}}_i\right)^{\mathrm{T}}\\ \dfrac{\partial \mathscr{L}}{\partial \boldsymbol{W}^{\mathrm{o}}_i} = \dfrac{\partial \mathscr{L}}{\partial \boldsymbol{f}^{\mathrm{o}}_{i+1}}\dfrac{\partial \boldsymbol{f}^{\mathrm{o}}_{i+1}}{\partial \boldsymbol{g}^{\mathrm{o}}_i}\dfrac{\partial \boldsymbol{g}^{\mathrm{o}}_i}{\partial \boldsymbol{W}^{\mathrm{o}}_i} = \left(\boldsymbol{f}^{\mathrm{o}}_i\right)^{\mathrm{T}}\dfrac{\partial \mathscr{L}}{\partial \boldsymbol{f}^{\mathrm{o}}_{i+1}}\sigma'\left(\boldsymbol{f}^{\mathrm{o}}_i\boldsymbol{W}^{\mathrm{o}}_i\right)\end{cases} & i < N_\mathrm{o}+1\\ \begin{pmatrix}\dfrac{\partial \mathscr{L}}{\partial \boldsymbol{f}^{\mathrm{o},\phi}_{N_\mathrm{o}+1}}\\ \dfrac{\partial \mathscr{L}}{\partial \boldsymbol{f}^{\mathrm{o},a}_{N_\mathrm{o}+1}}\end{pmatrix} = \boldsymbol{M}^{\mathrm{T}}\begin{pmatrix}\dfrac{\partial \mathscr{L}}{\partial \phi(\boldsymbol{r})}\\ \dfrac{\partial \mathscr{L}}{\partial a(\boldsymbol{r})}\end{pmatrix} & i = N_\mathrm{o}+1\end{cases}, \tag{S10}$$

$$\begin{cases}\begin{cases}\dfrac{\partial \mathscr{L}}{\partial \boldsymbol{f}^{\mathrm{s}}_i} = \dfrac{\partial \mathscr{L}}{\partial \boldsymbol{f}^{\mathrm{s}}_{i+1}}\dfrac{\partial \boldsymbol{f}^{\mathrm{s}}_{i+1}}{\partial \boldsymbol{g}^{\mathrm{s}}_i}\dfrac{\partial \boldsymbol{g}^{\mathrm{s}}_i}{\partial \boldsymbol{f}^{\mathrm{s}}_i} = \dfrac{\partial \mathscr{L}}{\partial \boldsymbol{f}^{\mathrm{s}}_{i+1}}\sigma'\left(\boldsymbol{f}^{\mathrm{s}}_i\boldsymbol{W}^{\mathrm{s}}_i\right)\left(\boldsymbol{W}^{\mathrm{s}}_i\right)^{\mathrm{T}}\\ \dfrac{\partial \mathscr{L}}{\partial \boldsymbol{W}^{\mathrm{s}}_i} = \dfrac{\partial \mathscr{L}}{\partial \boldsymbol{f}^{\mathrm{s}}_{i+1}}\dfrac{\partial \boldsymbol{f}^{\mathrm{s}}_{i+1}}{\partial \boldsymbol{g}^{\mathrm{s}}_i}\dfrac{\partial \boldsymbol{g}^{\mathrm{s}}_i}{\partial \boldsymbol{W}^{\mathrm{s}}_i} = \left(\boldsymbol{f}^{\mathrm{s}}_i\right)^{\mathrm{T}}\dfrac{\partial \mathscr{L}}{\partial \boldsymbol{f}^{\mathrm{s}}_{i+1}}\sigma'\left(\boldsymbol{f}^{\mathrm{s}}_i\boldsymbol{W}^{\mathrm{s}}_i\right)\end{cases} & i < N_\mathrm{s}+1\\ \dfrac{\partial \mathscr{L}}{\partial \boldsymbol{f}^{\mathrm{s}}_{N_\mathrm{s}+1}} = \boldsymbol{T}^{\mathrm{T}}\dfrac{\partial \mathscr{L}}{\partial \boldsymbol{k}} & i = N_\mathrm{s}+1\end{cases}. \tag{S11}$$

Section 2. Analysis of loss function composition and parameter selection

To evaluate the effectiveness of the loss function design in USDPC, we performed a series of comparative simulations. We analyzed three loss function configurations: MSE, a combination of MSE and TV, and the proposed composite loss integrating MSE, TV, and SSIM. The simulation results substantiate the specific role and necessity of each term. As shown in Fig. S1(a), reconstructions using MSE loss alone suffer from significant artifacts and errors. The introduction of the TV regularization term markedly improves spatial consistency and reconstruction quality. While the inclusion of the SSIM term yields a final accuracy comparable to MSE+TV, it provides a dramatic improvement in computational efficiency. As illustrated in Fig. S1(b), the MSE+TV configuration requires approximately 30,000 iterations to reach convergence, whereas the addition of the SSIM term reduces this requirement to roughly 2,000 iterations — a 15-fold acceleration. These findings validate that the

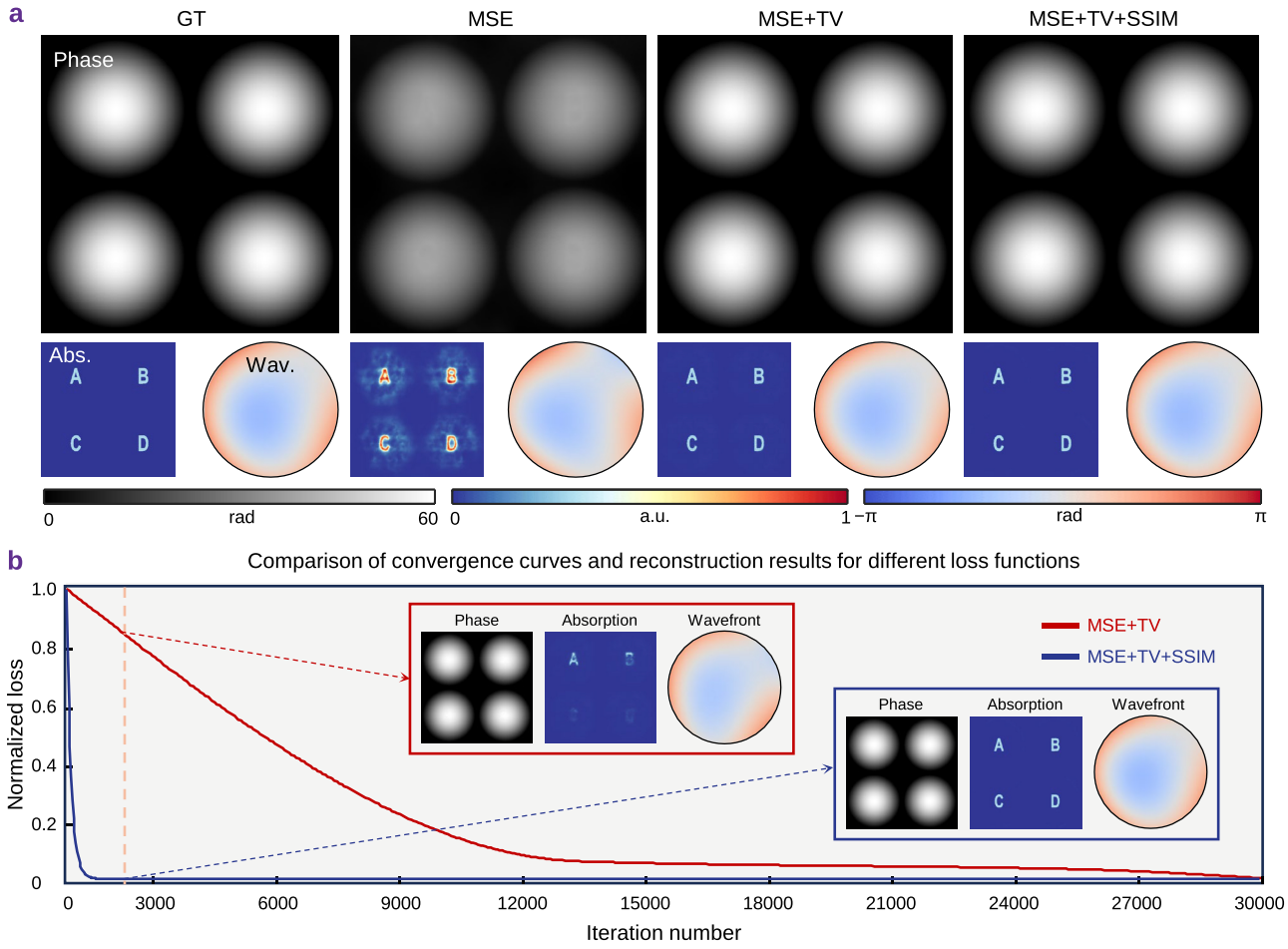


Fig. S1 | Comparative analysis of reconstruction performance across different loss function configurations. (a) Reconstructed phase, absorption, and aberration maps of a microlens array utilizing MSE, MSE+TV, and MSE+TV+SSIM loss functions. The ground truth (GT) is provided for comparison. (b) Normalized loss convergence curves comparing the standard MSE+TV approach (red) against the proposed MSE+TV+SSIM composite loss (blue). Insets display the intermediate reconstruction results at the 2,000th iteration, highlighting the superior convergence speed and early-stage fidelity afforded by the SSIM regularization term.

integration of TV and SSIM regularization is essential for achieving both high-fidelity results and rapid convergence.

Following the comparison of different loss function compositions, we further investigated the influence of the weighting parameters in the hybrid loss. Numerical simulations were performed using simulated HeLa cells containing phase, absorption, and optical aberration, as shown in Fig. S2(a). We first evaluated the influence of the TV weighting parameter τ. Reconstruction results obtained with $\tau = 10^{-1}$, $\tau = 10^{-2}$, and $\tau = 10^{-3}$ are shown in Fig. S2(b). When $\tau = 10^{-1}$, the TV regularization is overly strong, resulting in excessive smoothing and loss of fine structural details, yielding a phase RMSE of 2.46% and an SSIM of 0.6869. In contrast, when $\tau = 10^{-3}$, the regularization becomes insufficient to suppress discretization and pixelation artifacts, resulting in a phase RMSE of 1.01% and an SSIM of 0.8476. The best reconstruction performance is achieved with $\tau = 10^{-2}$, which provides the lowest RMSE (0.79%) and the highest SSIM (0.9551), indicating an appropriate balance between artifact suppression and detail preservation.

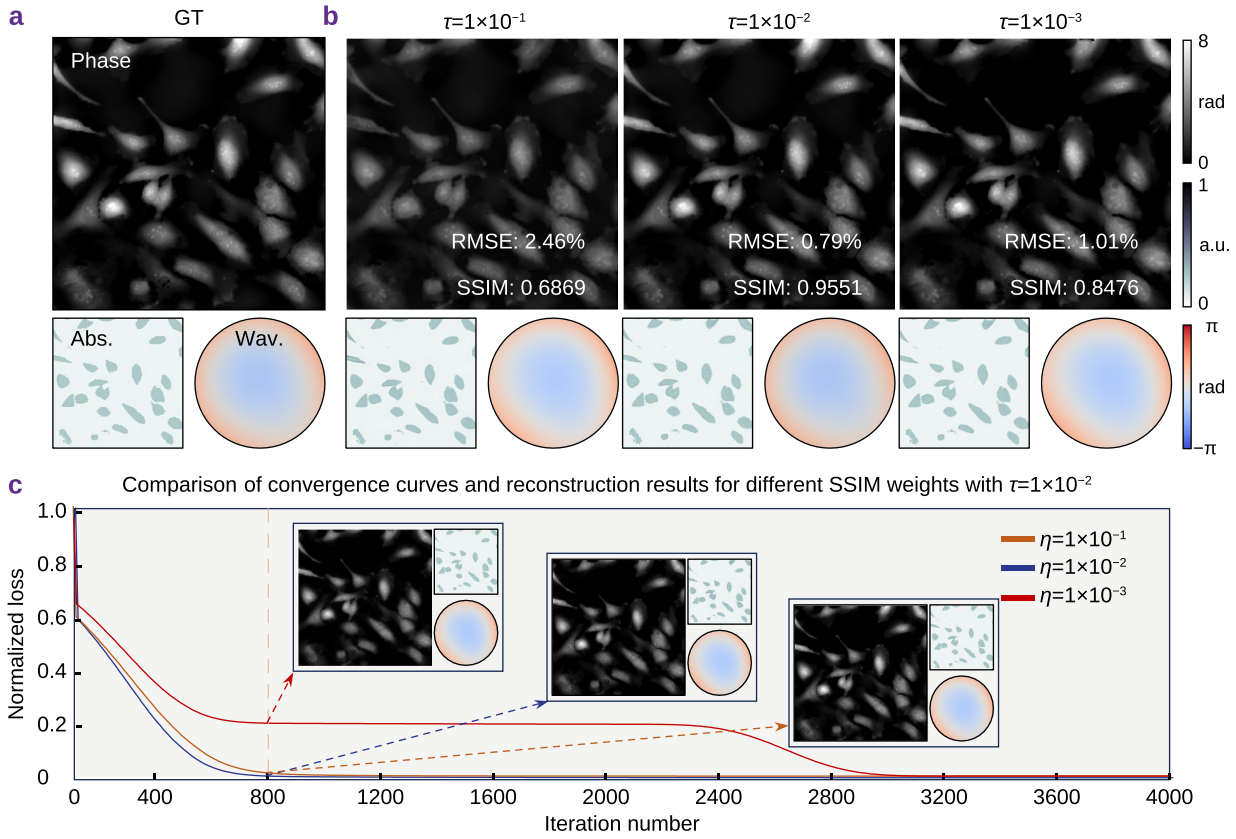


Fig. S2 | Analysis of the weighting parameters in the hybrid loss function. (a) Ground-truth phase, absorption, and optical aberration distributions of the simulated HeLa cells used in the numerical simulations. (b) Reconstruction results obtained using different TV weighting parameters, including the reconstructed phase, absorption, and optical aberration. (c) Convergence curves obtained with different SSIM weighting parameters.

The influence of the SSIM weighting parameter η was subsequently analyzed with $\tau = 10^{-2}$, and the corresponding convergence curves are shown in Fig. S2(c). Since the primary role of the SSIM term is to accelerate optimization, different values of η have little influence on the final reconstruction accuracy but noticeably affect the convergence rate. When $\eta = 10^{-3}$, the contribution of the SSIM loss is too weak to provide an effective convergence acceleration. Increasing η to 10^{-2} substantially improves the convergence speed. A further increase to 10^{-1} provides only slightly additional acceleration while placing greater emphasis on the SSIM term during optimization. To preserve the physical consistency of the optimization by allowing the intensity-based MSE loss to remain dominant, excessively large values of η are therefore avoided. Overall, the proposed framework exhibits moderate sensitivity to the TV weighting parameter but is relatively insensitive to the choice of the SSIM weighting parameter. Based on extensive empirical evaluation, both τ and η were set to 10^{-2} throughout this work, providing a favorable compromise between reconstruction accuracy and computational efficiency. Although the optimal values may vary slightly under different imaging conditions, satisfactory performance can be achieved over a relatively broad parameter range without extensive parameter tuning.

Section 3. Analysis of coordinate encoding and MLP depth

To examine the choice of coordinate encoding and network depth in USDPC, numerical simulations were performed using simulated HeLa cells containing phase, absorption, and optical aberration. The ground-truth phase distribution and the corresponding four intensity measurements are shown in Fig. S3(a). We first compared three coordinate encoding schemes: positional encoding[S3], Gaussian encoding[S4], and the radial encoding used in this work. Positional encoding is defined as

$$\gamma_{\mathrm{pos}}(\boldsymbol{R}) = \left[\boldsymbol{R}, \cos(2^0\pi\boldsymbol{R}), \sin(2^0\pi\boldsymbol{R}), \cdots, \cos(2^{L-1}\pi\boldsymbol{R}), \sin(2^{L-1}\pi\boldsymbol{R})\right]. \tag{S12}$$

Gaussian encoding is expressed as

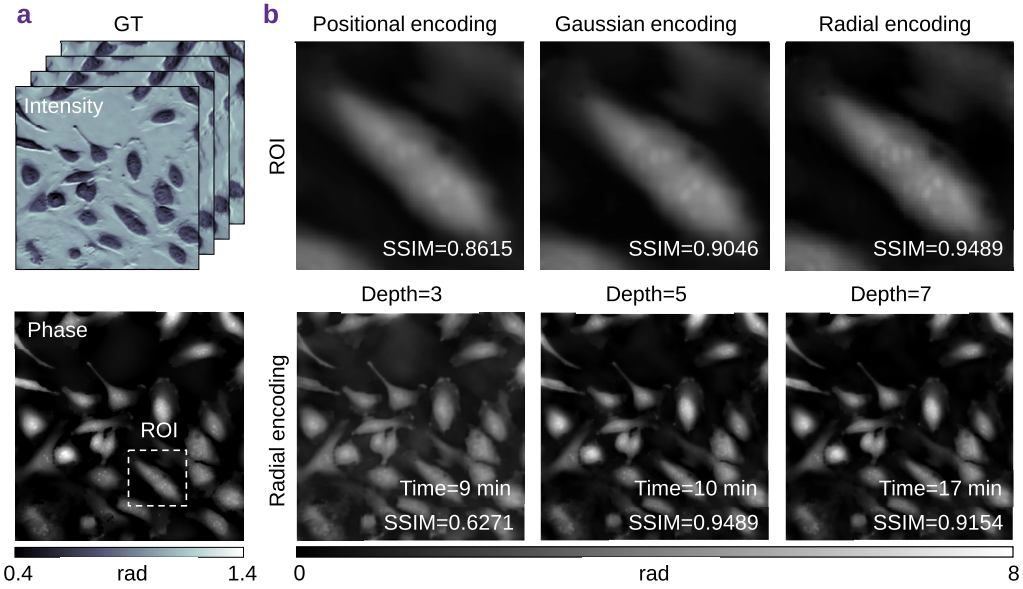


Fig. S3 | Numerical analysis of coordinate encoding strategies and MLP depth. (a) Ground-truth phase distribution of the simulated HeLa cells and the corresponding four simulated intensity measurements. (b) Reconstruction results obtained using different encoding strategies, together with the phase reconstruction results obtained using different MLP depths under the radial encoding strategy.

$$\gamma_{\text{gauss}}(\boldsymbol{R}) = \left[\boldsymbol{R}, \cos(2\pi \boldsymbol{R}\boldsymbol{N}) , \sin(2\pi \boldsymbol{R}\boldsymbol{N})\right] , \tag{S13}$$

where $\boldsymbol{R}$ denotes the normalized spatial coordinates, L is the number of encoding frequencies, and $\boldsymbol{N} \sim \mathcal{N}(\mu = 0, \sigma^2 = a)$ is a Gaussian random sampling matrix with variance a. The radial encoding follows Eq. (8) in the main text and generates multi-directional frequency components through a set of rotation matrices. As shown by the enlarged region in Fig. S3(b), radial encoding provides more accurate recovery of cell boundaries and fine structural features than positional and Gaussian encoding, yielding the highest phase SSIM among the three schemes. It was therefore adopted throughout this work.

We next evaluated MLPs with 3, 5, and 7 hidden layers while keeping all other settings unchanged. The three-layer network required less computation but lacked sufficient representation capacity, resulting in a phase SSIM of 0.6271. Increasing the depth to five layers substantially improved the reconstruction quality, with an SSIM of 0.9489 and a reconstruction time of approximately 10 min. A seven-layer network increased the reconstruction time to approximately 17 min but did not provide a corresponding improvement in accuracy. Therefore, the five-layer MLP was selected as a practical balance between representation capability and computational efficiency.

Section 4. Robustness analysis of USDPC for reconstructing large-phase samples

The performance of USDPC was validated on microlens arrays with peak phase values up to 60 rad. To further evaluate its robustness under stronger nonlinear conditions, we performed comparative simulations with conventional DPC[S5] and iterative DPC[S6] using simulated microlens arrays with peak phase values of 30, 60, 80, and 100 rad. The corresponding intensity images were generated using the strict partially coherent forward model described by Eq. (1) in the main text under asymmetric semicircular illumination. The reconstruction results are shown in Fig. S4.

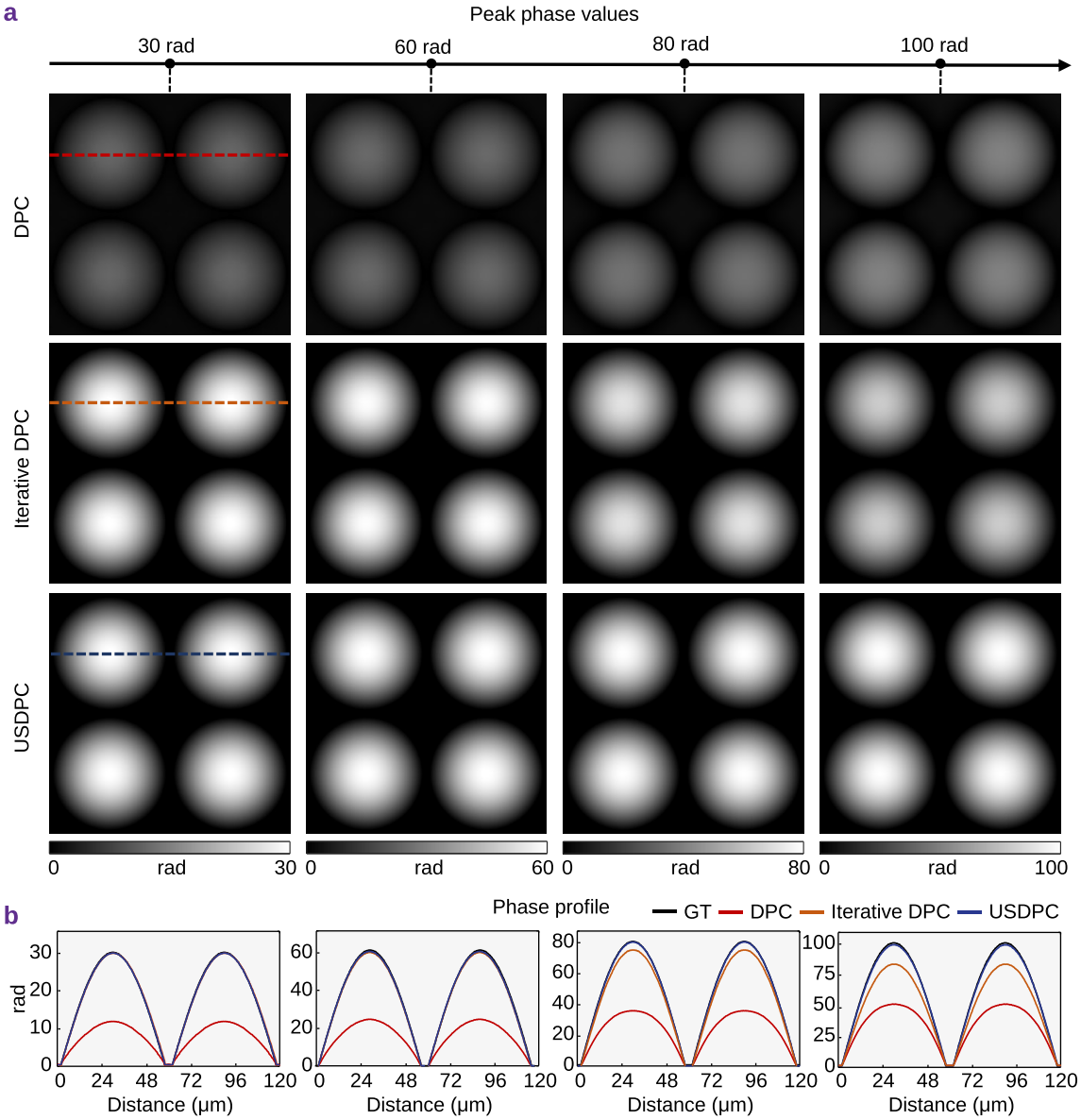


Fig. S4 | Comparative reconstruction of microlens arrays with increasing phase amplitudes using conventional DPC, iterative DPC, and USDPC. (a) Simulation results of microlens arrays with peak phase values of 30, 60, 80, and 100 rad. (b) Quantitative phase profiles extracted from the reconstructed microlens arrays.

As shown in the first row of Fig. S4(a), conventional DPC fails to recover quantitative phase information in all cases and produces severely underestimated phase values. This behavior is expected because even the lowest tested phase delay (30 rad) far exceeds the validity range of the weak object approximation[S7] (typically < 0.5 rad), upon which conventional DPC is based. Iterative DPC substantially improves the reconstruction accuracy at 30 rad and 60 rad. However, its performance progressively deteriorates as the phase delay increases, exhibiting noticeable reconstruction errors at 80 rad and 100 rad, as shown in the second row of Fig. S4(a). In contrast, USDPC maintains accurate phase reconstruction across the entire tested range, including the most challenging 100 rad case, with reconstructed phase distributions closely matching the ground truth. These observations are further confirmed by the phase profiles shown in Fig. S4(b). Conventional DPC consistently underestimates the phase, whereas the reconstruction error of iterative DPC increases with the phase values. By comparison, the phase profiles recovered by USDPC remain in close agreement with the ground truth throughout the investigated phase range.

To further investigate the practical operating range of USDPC under more realistic imaging conditions, we constructed a complex transmission phantom containing simultaneously large phase variations, non-negligible absorption, and unknown

optical aberrations (Fig. S5(a)). Unlike the pure-phase microlens simulations, this phantom combines microlens-based phase structures with alphabet-patterned absorption features while introducing optical aberrations. The phase magnitude was gradually scaled while all other imaging parameters remained unchanged, allowing the reconstruction performance to be evaluated over an extended dynamic range. As shown in Fig. S5(b) and S5(c), USDPC accurately recovers both the phase and absorption distributions while simultaneously compensating for the unknown optical aberration for phase delays up to approximately 130 rad. When the maximum phase delay is further increased to 150 rad, noticeable reconstruction artifacts begin to appear, accompanied by crosstalk between the recovered phase and absorption channels. These results indicate that USDPC substantially extends the quantitative operating range of DPC-based phase imaging and maintains reliable reconstruction performance for phase delays up to approximately 130 rad under the current nonlinear inversion framework.

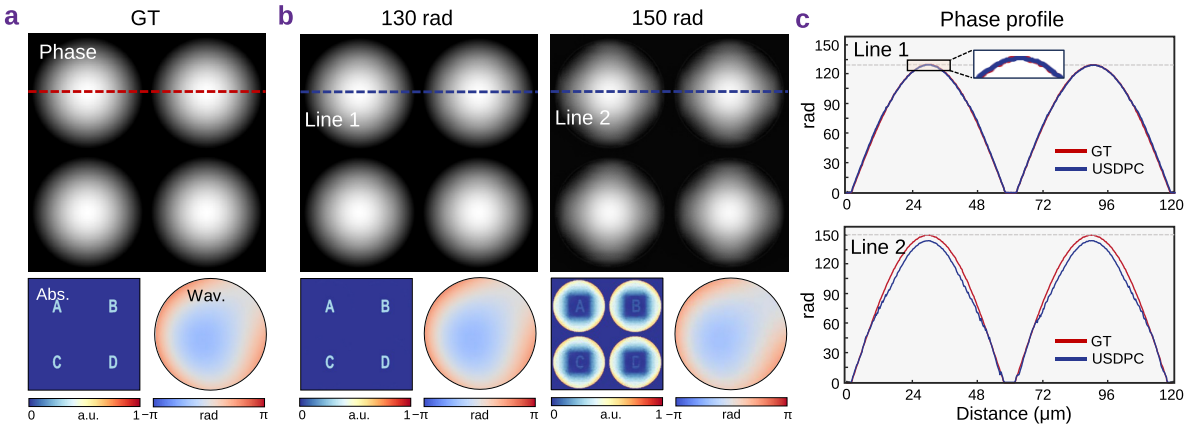


Fig. S5 | Numerical validation of the effective phase reconstruction range of USDPC. (a) Ground truth of complex transmission phantom consisting of a microlens-encoded phase component and an alphabet-pattern amplitude component, shown alongside the simulated optical aberration. (b) USDPC reconstructions under identical system configurations for maximum phase delays of 130 rad and 150 rad. (c) Phase line profile along the marked line in (a) and (b).

In addition, the computational performance of the three reconstruction methods was compared under the same hardware configuration (see main text), as summarized in Table S1. Conventional DPC reconstructs a standard 512×512 image patch in approximately 1 s but is limited to a recoverable phase range of about 0.5 rad. Iterative DPC extends the recoverable phase range to approximately 60 rad with a reconstruction time of about 1 min. In comparison, USDPC requires approximately 10 min to converge, while further extending the recoverable phase range to approximately 130 rad and simultaneously enabling blind aberration correction and absorption reconstruction. Although the neural-field optimization introduces additional computational cost, it provides substantially improved reconstruction capability under challenging conditions involving large phase variations and unknown optical aberrations.

Table S1 | Comparison of reconstruction capability and computational efficiency of different DPC reconstruction methods.

Method	Phase range	Aberration correction	Absorption reconstruction	Reconstruction time
DPC[S5]	~ 0.5 rad	×	✓	~ 1 s
Iterative DPC[S6]	~ 60 rad	×	×	~ 1 min
USDPC	~ 130 rad	✓	✓	~ 10 min

Section 5. Numerical characterization of the aberration correction capability of USDPC

To characterize the aberration correction capability of USDPC[S8], we first evaluated its performance under increasing aberration magnitudes using two representative specimens: a microlens phantom dominated by low spatial frequencies and a resolution target containing abundant high-frequency structures. The corresponding ground-truth phase distributions and simulated aberrations are shown in Fig. S6(a) and S6(c). For the microlens phantom, USDPC accurately recovered both the specimen

phase and the optical aberration for aberration amplitudes up to ±8 rad (Fig. S6(b)). When the aberration amplitude increased to ±12 rad, the reconstruction failed to converge to the correct solution, resulting in noticeable structural distortions and inaccurate aberration estimation. By comparison, the resolution target exhibited a lower tolerance to optical aberrations because of its richer high-frequency content. As shown in Fig. S6(d), reliable reconstruction was achieved up to ±4 rad, whereas increasing the aberration amplitude to ±8 rad introduced pronounced reconstruction artifacts and high-frequency noise. These results indicate that the effective aberration correction capability of USDPC is specimen-dependent and governed by the spatial-frequency complexity of the object rather than representing a fixed intrinsic limit of the proposed framework. To further investigate the origin of this limitation, we also evaluated more expressive network configurations by increasing both the depth of the multilayer perceptron and the Zernike expansion order used to represent the pupil aberration. However, these modifications provided only marginal improvement while introducing additional computational cost and optimization complexity. This suggests that the degradation under strong aberrations is not primarily limited by the representational capacity of the neural-field model or the Zernike parameterization, but rather by the intrinsic difficulty of the blind inverse problem itself. As the aberration magnitude increases, the coupling between the specimen phase, particularly its high-spatial-frequency components, and the pupil aberration becomes progressively stronger, leading to increased ambiguity in disentangling these two unknown quantities. Consequently, the optimization becomes increasingly non-convex, making the joint estimation of the specimen and the aberration more susceptible to convergence toward suboptimal local minima.

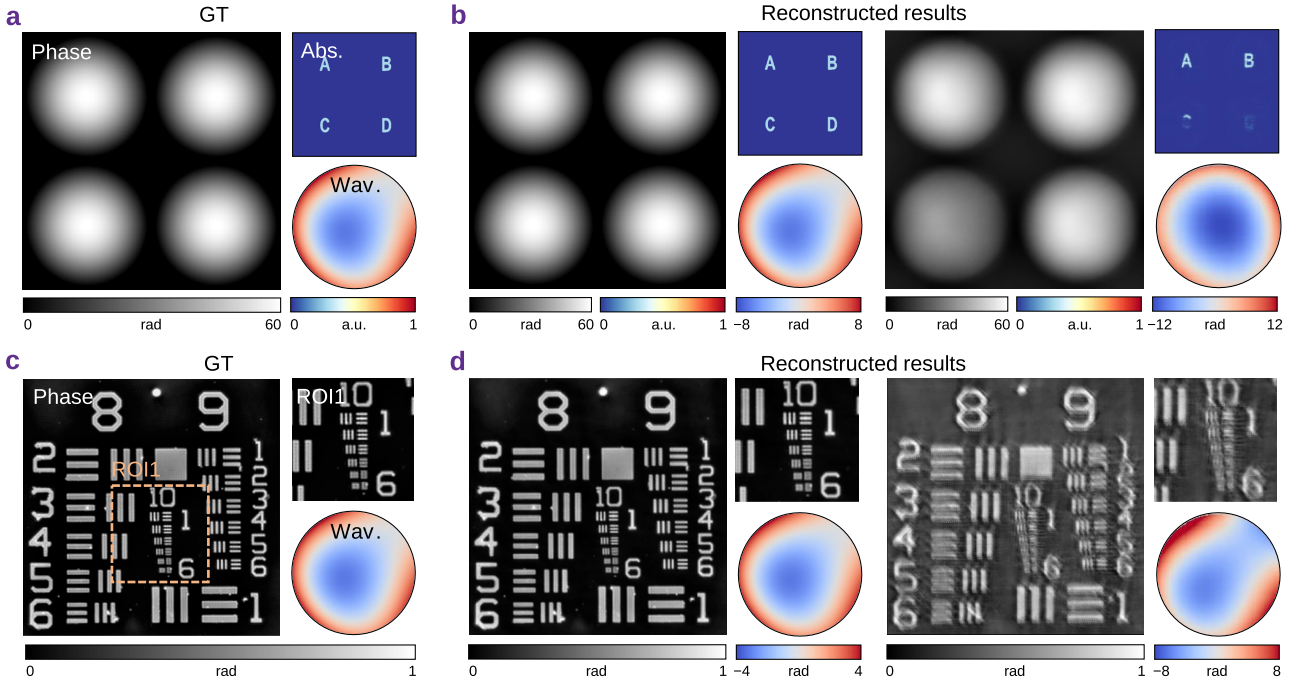


Fig. S6 | Numerical characterization of the aberration correction capability of USDPC. (a) Ground-truth phase, absorption, and optical aberration of the simulated microlens phantom. (b) USDPC reconstructions under different aberration magnitudes. Accurate reconstruction is achieved at ± 8 rad, whereas noticeable artifacts appear at ± 12 rad. (c) Ground-truth phase distribution and optical aberration of the simulated resolution target. (d) Reconstruction results for the resolution target under different aberration magnitudes. Reliable correction is achieved at ± 4 rad, whereas the reconstruction degrades at ± 8 rad.

To further evaluate the aberration correction capability of USDPC under increasingly complex aberration conditions, we considered three aberration models composed of Zernike modes 4-15, 16-28, and 29-36 using simulated HeLa cells, providing a more representative assessment for practical biological imaging. For a fair comparison, all aberration models were normalized to the same root-mean-square (RMS) wavefront error of 0.95 rad. The ground-truth phase distributions and corresponding aberration wavefronts are shown in Fig. S7(a). During reconstruction, the aberration composition was assumed to be unknown. Therefore, USDPC consistently employed a complete Zernike basis spanning modes 4-36 for all three cases, allowing the algorithm to estimate the aberration without prior knowledge of the active Zernike modes. The reconstruction results are presented in Fig. S7(b). For aberrations composed of Zernike modes 4-15, USDPC accurately recovered both the specimen phase and the wavefront, yielding an RMSE of 0.27% and an SSIM of 0.9478. Similar perfor-

mance was achieved for Zernike modes 16-28, with an RMSE of 0.79% and an SSIM of 0.9113. In contrast, reconstruction quality deteriorated markedly for aberrations composed of Zernike modes 29-36, where the RMSE increased to 23.02% and the SSIM decreased to 0.1604. The recovered wavefronts and the corresponding Zernike coefficients further confirm accurate aberration estimation for the first two groups, whereas substantial deviations are observed for modes 29-36. These results suggest that USDPC can reliably recover optical aberrations represented by Zernike modes up to 28 (corresponding to the seventh radial order). Beyond this range, the increasing complexity of the aberration significantly complicates the blind inverse problem, leading to degraded aberration estimation and phase reconstruction.

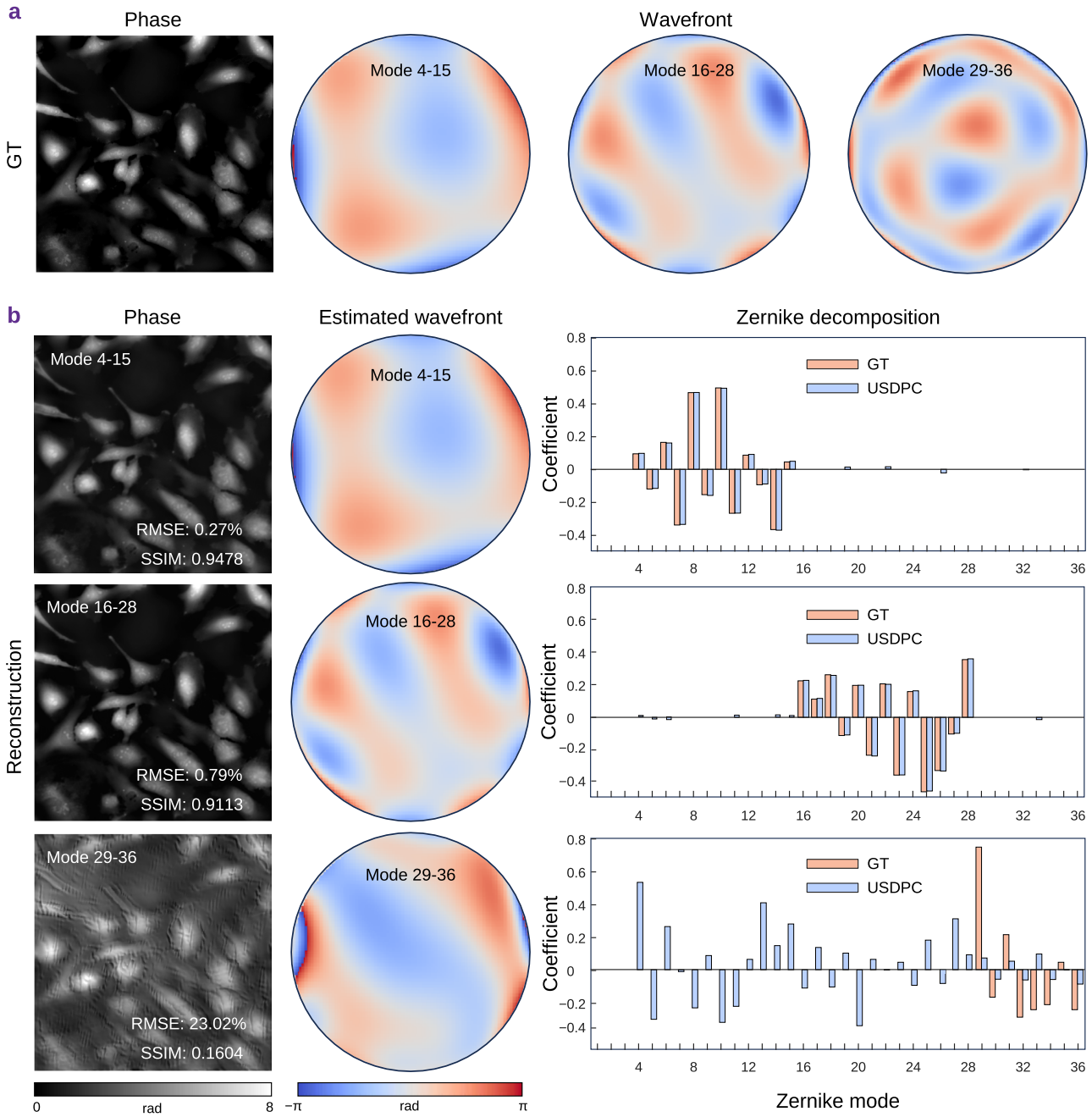


Fig. S7 | Numerical characterization of the aberration correction capability of USDPC under increasingly complex aberrations. (a) Ground-truth phase distribution and simulated aberration wavefronts composed of Zernike modes 4-15, 16-28, and 29-36, respectively. All aberrations were normalized to the same RMS wavefront error (0.95 rad). (b) Reconstruction results obtained with USDPC, including the recovered phase distributions, aberration wavefronts, and comparisons between the ground-truth and reconstructed Zernike coefficients.

Section 6. Numerical evaluation of the noise robustness of USDPC

To evaluate the robustness of USDPC to measurement noise[S9], Gaussian noise was added to the simulated intensity measurements at signal-to-noise ratios (SNRs) of 40, 20, 15, and 10 dB. The simulated HeLa cells were used as the test object, with sample phase, absorption, and optical aberration jointly included in the forward model. The ground-truth distributions and the corresponding noise-free intensity measurements are shown in Fig. S8(a), and the reconstruction results under different noise levels are presented in Fig. S8(b). At an SNR of 40 dB, USDPC accurately recovers the phase, absorption, and optical aberration, yielding a phase SSIM of 0.9512 and an RMSE of 0.85%. At 20 dB, the reconstruction remains stable, with an SSIM of 0.9358 and an RMSE of 1.48%. As the SNR decreases to 15 dB, reconstruction errors begin to become more evident, with the SSIM decreasing to 0.7882 and the RMSE increasing to 4.77%. At 10 dB, pronounced noise artifacts appear in the reconstructed phase and absorption, while the recovered aberration exhibits reduced contrast and underestimated amplitude. The corresponding phase SSIM and RMSE are 0.4954 and 10.68%, respectively. These results show that the reconstruction accuracy of USDPC gradually degrades as the measurement noise increases. Nevertheless, the method maintains reliable reconstruction at SNRs of 20 dB and above.

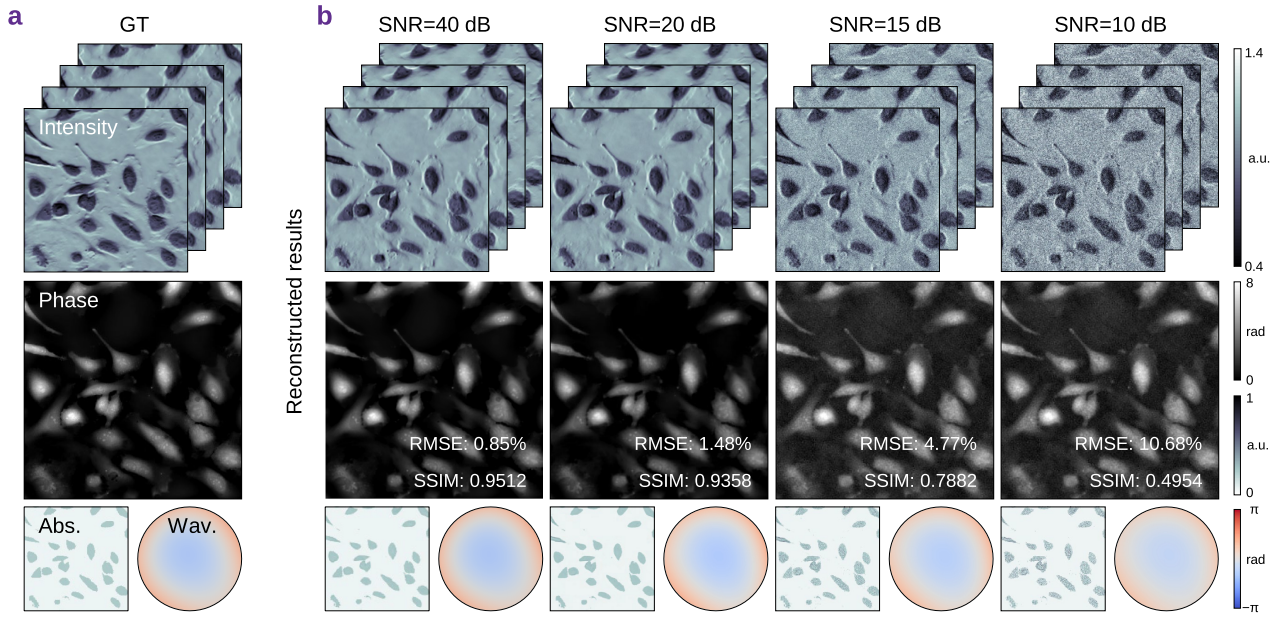


Fig. S8 | Numerical evaluation of the influence of measurement noise on USDPC reconstruction. (a) Ground-truth phase, absorption, and optical aberration distributions, together with the four noise-free intensity measurements generated by the partially coherent forward model. (b) Reconstruction results of USDPC obtained from measurements with SNRs of 40, 20, 15, and 10 dB.

Section 7. Analysis of the subregion partitioning and stitching strategy

To improve the computational efficiency of wide-field reconstruction while accurately accommodating spatially varying optical aberrations, the acquired intensity images were divided into multiple overlapping subregions for independent reconstruction. Each subregion was approximately 512×512 pixels, with an overlap of 50 pixels (approximately one-tenth of the subregion size) to provide sufficient shared information for seamless stitching. The reconstructed phase distributions in the overlapping region were combined using linear blending[S10]:

$$\phi(x) = [1 - w(x)]\phi_1(x) + w(x)\phi_2(x) \quad , \tag{S14}$$

where $\phi_1(x)$ and $\phi_2(x)$ denote the reconstructed phase distributions of two adjacent subregions, and $w(x) \in [0,1]$ is a linearly varying weighting coefficient across the overlap region. To evaluate the stitching strategy, a representative boundary region is shown in Fig. S9(a). Direct concatenation introduces visible discontinuities because adjacent subregions are reconstructed independently. In contrast, linear blending produces a smooth transition across the overlap region and effectively suppresses boundary artifacts.

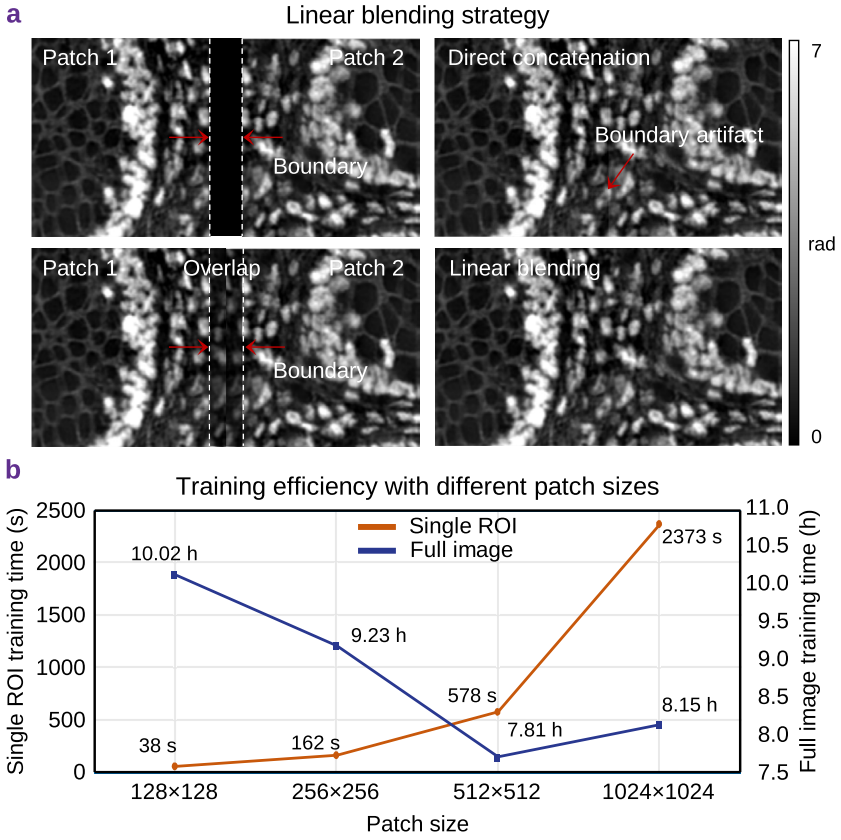


Fig. S9 | Evaluation of the subregion partitioning and stitching strategy. (a) Comparison of direct concatenation and linear blending in the overlapping region between adjacent subregions. (b) Reconstruction time as a function of subregion size, including the reconstruction time for a single subregion and the total reconstruction time for the full field of view.

In addition, we analyzed the influence of subregion size on computational efficiency. Reducing the subregion size shortens the reconstruction time for an individual subregion but increases the total number of subregions required to cover the full field of view. For the experimental field of view of 3872×2764 pixels, the image was partitioned into overlapping patches with sizes of 128×128, 256×256, 512×512, and 1024×1024 pixels. Because the image dimensions are not exact multiples of these patch sizes, the patches along the image boundaries were slightly resized to ensure complete coverage of the field of view. Taking the 512×512 configuration as an example, the image was divided into a 8×6 grid with a 50-pixel overlap between adjacent patches. Interior patches retained the nominal size, whereas only the boundary patches were adjusted to accommodate the remaining image area. The same strategy was applied to the other partitioning schemes, with the overlap width maintained at approximately one-tenth of the corresponding patch size. The computational performance of the four partitioning schemes is summarized in Fig. S9(b). For the 512×512 configuration, the average reconstruction time for a single patch was approximately 578 s, corresponding to a total reconstruction time of 7.81 h for the full field of view. Reducing the patch size substantially shortened the reconstruction time of individual patches but increased the total number of patches, leading to additional computational overhead. Consequently, the overall reconstruction time exhibits a non-monotonic dependence on patch size. Among the evaluated configurations, the 512×512 partitioning scheme provides the best balance between local reconstruction efficiency and the total computational cost, making it the most suitable choice for wide-field reconstruction.

Section 8. Evaluation metrics for assessing the image quality in quantitative phase imaging

To quantitatively evaluate the image quality of histological sections reconstructed via DPC and USDPC imaging, we adopt three complementary image quality assessment metrics: the Natural Image Quality Evaluator (NIQE)[S11], the Energy of Gradient (EOG)[S12], and the Contrast-to-Noise Ratio (CNR)[S13].

NIQE is a fully blind image quality assessment method that quantifies the deviation of an input image from the statistical regularities of natural scenes, without requiring any reference images, human opinion scores, or knowledge of distortion

types. This makes it particularly suitable for evaluating reconstruction or super-resolution results where ground truth is unavailable. Formally, the NIQE score is computed as the Mahalanobis distance between the natural scene statistics (NSS) features extracted from the test image and those from a high-quality natural image corpus:

$$D_{\mathrm{NIQE}} = \sqrt{(\boldsymbol{\mu}_{\phi} - \boldsymbol{\mu}_{\mathrm{ref}})^{\mathrm{T}} \left(\frac{\boldsymbol{\nu}_{\phi} + \boldsymbol{\nu}_{\mathrm{ref}}}{2} \right)^{-1} (\boldsymbol{\mu}_{\phi} - \boldsymbol{\mu}_{\mathrm{ref}})} \,, \tag{S15}$$

where $\boldsymbol{\mu}_{\phi}$ and $\boldsymbol{\nu}_{\phi}$ are the mean vector and covariance matrix of NSS features extracted from the test image, $\boldsymbol{\mu}_{\mathrm{ref}}$ and $\boldsymbol{\nu}_{\mathrm{ref}}$ correspond to those of the reference natural image set. In this metric, a lower NIQE score indicates better image quality, typically associated with higher sharpness and more natural image characteristics.

The EOG metric is employed to evaluate image clarity by measuring the magnitude of local intensity gradients, which are typically more prominent at object edges in sharper images. Specifically, EOG quantifies image sharpness by computing the first-order finite differences along the horizontal and vertical directions. It is defined as

$$D_{\mathrm{EOG}} = \frac{1}{MN} \sum_{x=1}^{M} \sum_{y=1}^{N} \left\{ [\nabla_x \phi(x,y)]^2 + [\nabla_y \phi(x,y)]^2 \right\} \,, \tag{S16}$$

where ∇_x and ∇_y denote the finite difference operations along the x and y directions, respectively. M and N represent the number of pixels in the horizontal and vertical dimensions. A higher EOG score corresponds to improved image quality, reflecting enhanced sharpness.

The Contrast-to-Noise Ratio (CNR) was further employed to quantitatively evaluate the phase contrast relative to the background noise. It is defined as:

$$D_{\mathrm{CNR}} = \frac{\left| \mu_{\mathrm{obj}} - \mu_{\mathrm{bg}} \right|}{\sigma_{\mathrm{bg}}} \,, \tag{S17}$$

where μ_{obj} and μ_{bg} denote the mean phase values of object and background regions, respectively, and σ_{bg} represents the standard deviation of the background region. A higher CNR indicates stronger phase contrast and lower background noise, corresponding to better reconstruction quality.

Section 9. Quantitative phase imaging of unstained biological tissue section

We further extended the application of USDPC to quantitative phase imaging of unstained kidney tissue sections. As illustrated in Fig. S10(a), the USDPC method robustly reconstructed the complex morphology of the renal architecture, retrieving phase values as high as 20 rad. Compared to conventional DPC, which often suffers from artifacts in high-phase regimes, USDPC maintains high fidelity and spatial uniformity across the entire field of view. A comparative analysis of specific regions of interest (ROIs) (Fig. S10(b)) reveals that USDPC captures significantly finer structural details and provides enhanced contrast. These findings underscore the efficacy of USDPC in characterizing large-phase biological specimens and demonstrate its robustness in demanding experimental scenarios.

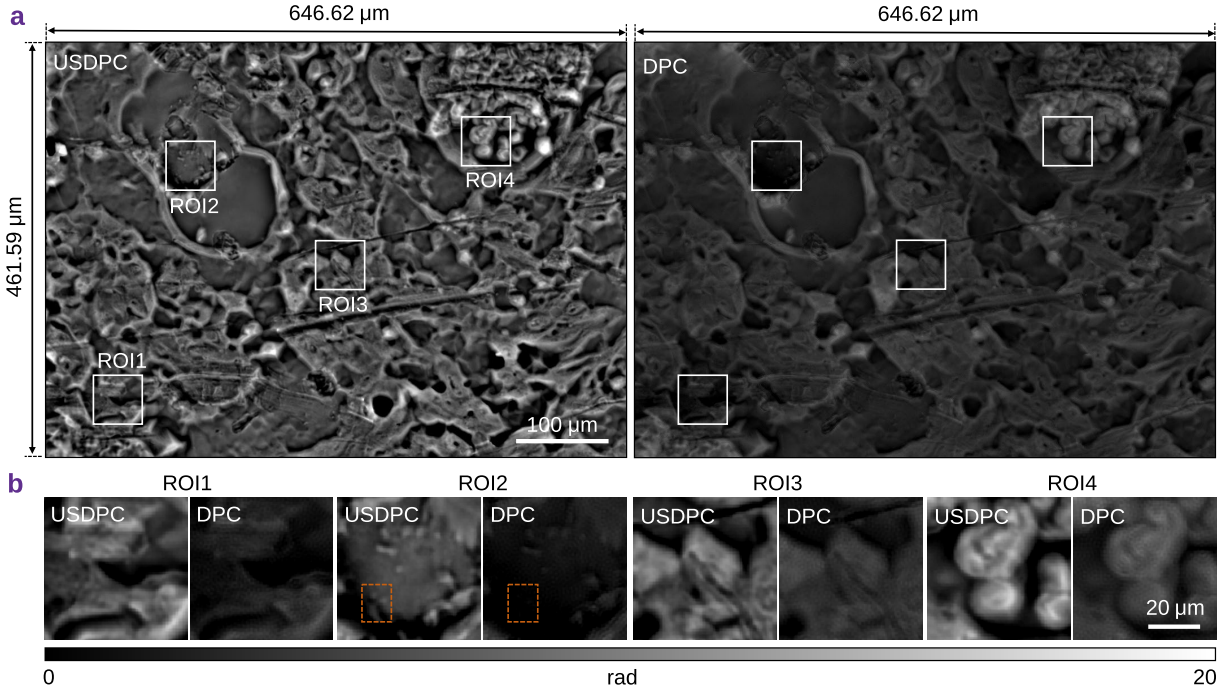


Fig. S10 | Quantitative phase imaging of unstained kidney tissue section. (a) Comparative full-field reconstructed phase maps using the proposed USDPC method and conventional DPC. (b) Magnified views of the regions of interest identified in (a), revealing significantly finer structural details and enhanced contrast compared to the conventional DPC results.

Section 10. Validation of USDPC under different objective numerical apertures

To evaluate the applicability of USDPC across different objective numerical apertures (NAs), phase imaging experiments were performed using 10×/0.4 NA, 20×/0.5 NA, and 40×/0.6 NA objectives. The corresponding reconstructions of the same area of cells are shown in Fig. S11(a). Two representative regions (ROI1 and ROI2) are enlarged in Fig. S11(b) for comparison. Increasing the objective NA extends the detectable spatial-frequency range and enables progressively finer subcellular features to be resolved in both ROIs.

However, a modest reduction in the local peak phase is also observed at higher NA. For an ideal thin object located at the focal plane, the quantitative phase is determined by the projected refractive index contrast and should not intrinsically depend on the objective NA. For a three-dimensional cell, however, the depth of field decreases approximately as $n\lambda/\mathrm{NA}^2$ with increasing NA. Consequently, a smaller fraction of the cell's axial extent may contribute effectively to the in-focus image, reducing the accumulated optical path length represented by the reconstructed phase. The lower peak phase at higher NA is therefore likely associated with the reduced depth of field. Overall, USDPC maintains stable reconstruction performance across the tested NA range while providing improved spatial resolution at higher NA.

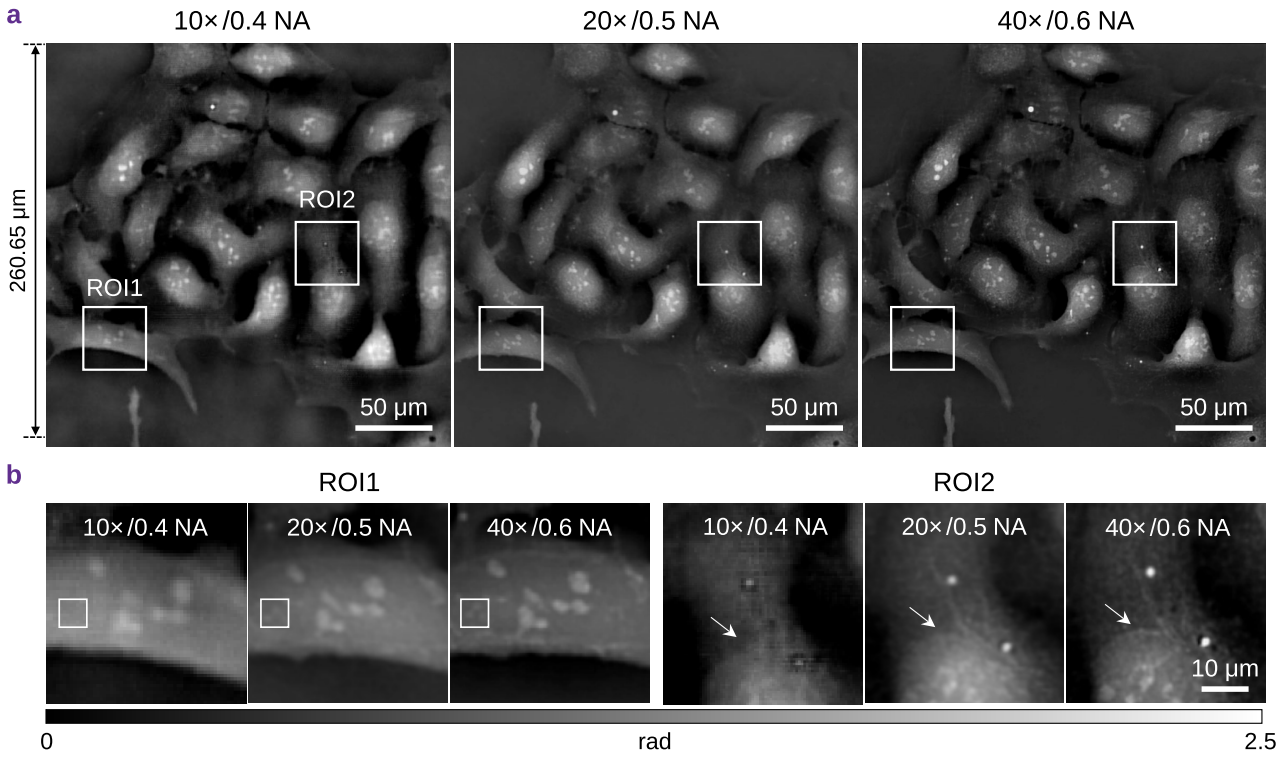


Fig. S11 | Experimental reconstruction results obtained using objective lenses with different NAs. (a) Reconstructed phase images of the same area of cells acquired using objective lenses with 10×/0.4 NA, 20×/0.5 NA, and 40×/0.6 NA, respectively. (b) Corresponding regions of interest extracted from the reconstructed phase images for detailed comparison.

Section 11. Analysis of the data requirement for stable USDPC reconstruction

The USDPC framework presented in the main text employs the standard four-frame DPC illumination scheme to provide sufficient measurement redundancy for solving the blind nonlinear inverse problem involving sample absorption, phase, and unknown optical aberrations. In this section, we further investigate the minimum measurement requirement through a series of numerical simulations.

We first consider the general reconstruction problem containing absorption, phase, and optical aberration. The ground-truth absorption and phase distributions are shown in Fig. S12(a), while the optical aberration is synthesized using a weighted combination of Zernike modes. Reconstruction was first performed using only two asymmetric illumination images (right and bottom), and the corresponding illumination patterns and simulated intensity measurements are shown in Fig. S12(b). As shown in Fig. S12(c) and S12(d), the recovered absorption suffers from pronounced phase-leakage artifacts, the reconstructed phase substantially underestimates the theoretical peak value of 60 rad, and the recovered Zernike coefficients deviate significantly from the ground truth, indicating an unstable solution. Increasing the measurement redundancy to three illumination images using a three-sector illumination pattern[S14] markedly improves the reconstruction quality (Fig. S12(e)). Nevertheless, slight crosstalk artifacts remain in the recovered absorption (Fig. S12(f)), and the reconstructed phase still exhibits slight deviations from the ground truth (Fig. S12(g)). These results indicate that three measurements remain insufficient to completely suppress the nonlinear coupling among absorption, phase, and optical aberration. In contrast, the standard four-frame acquisition scheme adopted in the main text provides sufficient measurement redundancy to enable stable and accurate blind reconstruction of the sample absorption, phase, and unknown optical aberrations within the proposed nonlinear inversion framework.

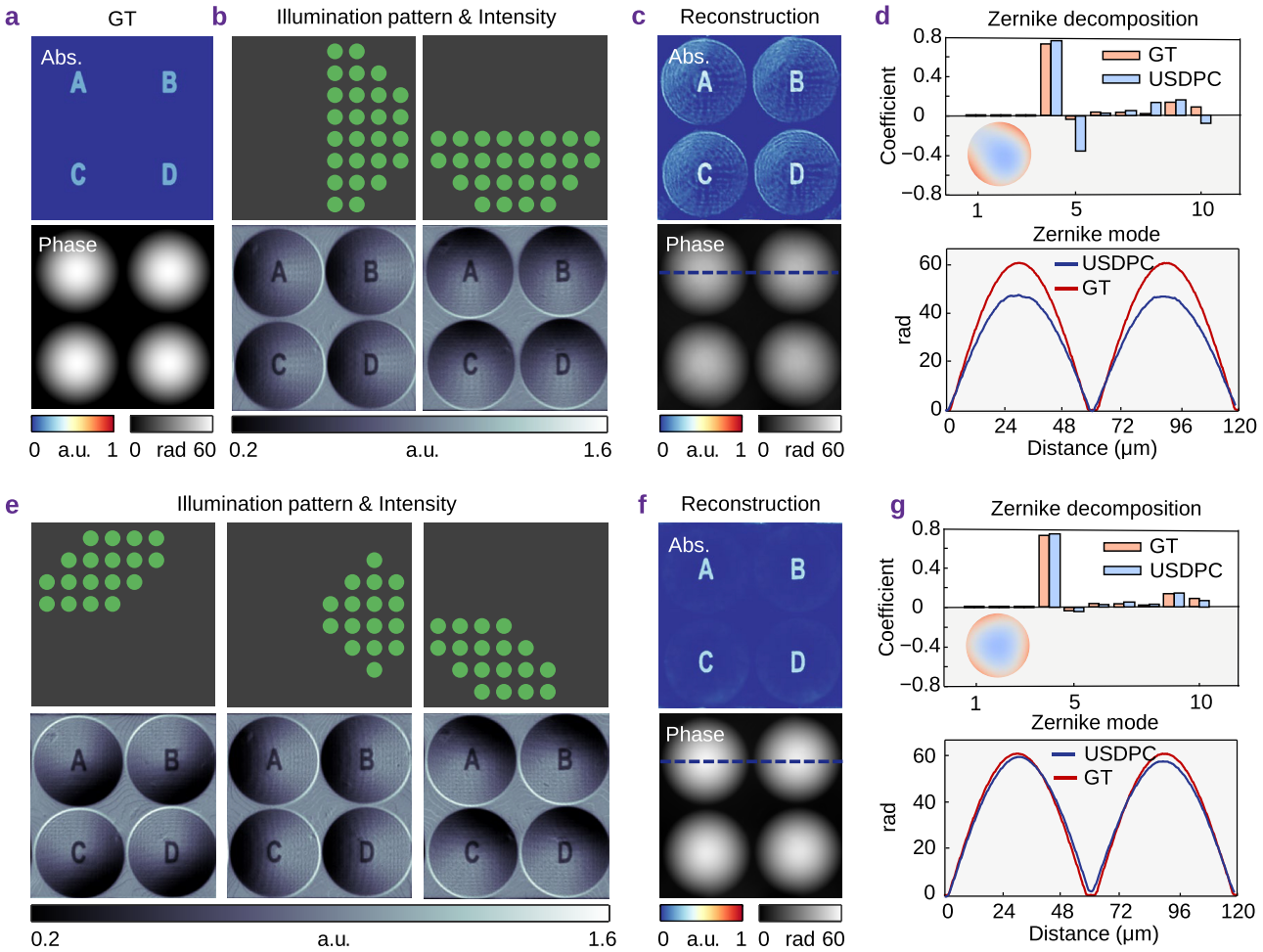


Fig. S12 | Simulation-based analysis of the data requirement for stable USDPC reconstruction. (a) Ground-truth absorption and phase of the simulated sample. (b) Two-frame illumination scheme and corresponding raw intensity measurements. (c) Reconstructed absorption and phase maps using the two-frame dataset. (d) Retrieved aberration map and phase profiles. (e) Three-frame illumination scheme and corresponding raw intensity measurements. (f) Reconstructed absorption and phase maps. (g) Retrieved aberration map and phase profiles.

To further investigate the influence of measurement redundancy on blind aberration correction, additional simulations were performed using a resolution target and microlens arrays containing only sample phase and optical aberration. The corresponding ground-truth phase distributions and optical aberrations are shown in Fig. S13(a). Reconstruction results obtained using different numbers of asymmetric illumination patterns are summarized in Fig. S13(b). When only two illumination images were used, strong coupling between the sample phase and optical aberration led to severe reconstruction errors for both samples. The recovered aberrations also deviated substantially from the ground truth, as reflected by the reconstructed Zernike coefficients. Using three asymmetric illumination images, USDPC was able to accurately decouple the sample phase from the optical aberration when these were the only two unknown quantities.

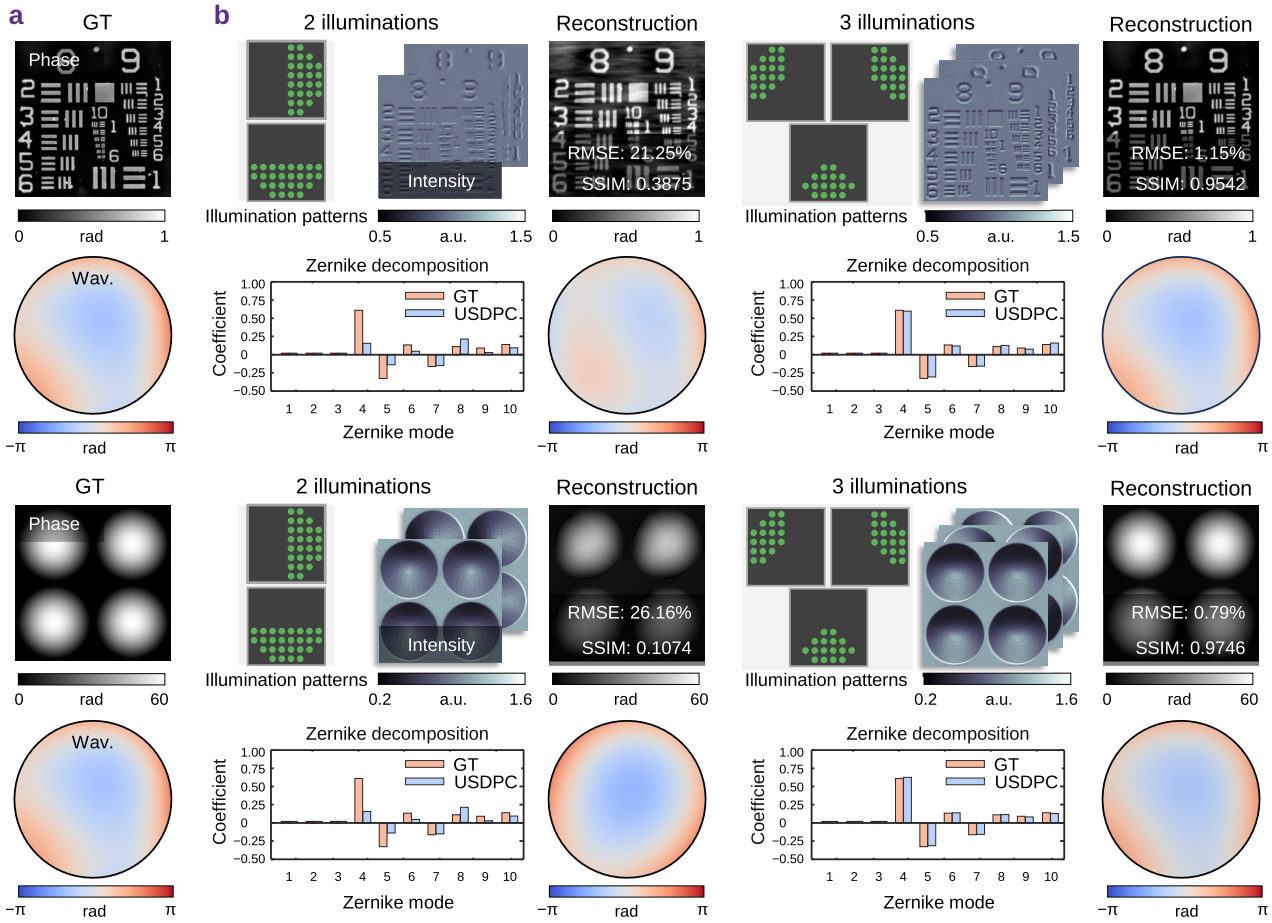


Fig. S13 | Numerical analysis of the influence of measurement redundancy on the decoupling of sample phase and optical aberration. (a) Ground-truth phase distributions of the resolution target and microlens arrays, together with the optical aberrations used in the simulations. (b) Reconstruction results obtained using different numbers of asymmetric illumination images, including the corresponding illumination patterns, simulated intensity measurements, reconstructed phase distributions, recovered optical aberrations, and comparisons between the reconstructed and ground-truth Zernike coefficients.

Combining these results, we conclude that the measurement redundancy requirement depends on the number of unknown variables in the inverse problem. For blind reconstruction involving only sample phase and optical aberration, three asymmetric illumination images are sufficient to achieve reliable decoupling. In the more general case considered throughout this work, where absorption, phase, and optical aberration are simultaneously unknown, four asymmetric illumination images are required to provide sufficient measurement redundancy for stable and accurate reconstruction.

References

S1. Paszke A, Gross S, Massa F et al. PyTorch: an imperative style, high-performance deep learning library. In *Proceedings of the 33rd International Conference on Neural Information Processing Systems* 721 (Curran Associates Inc., 2019). http://doi.org/10.5555/3454287.3455008.

S2. Nocedal J, Wright SJ. Numerical Optimization. 2nd ed. New York: Springer, 2006.

S3. Mildenhall B, Srinivasan PP, Tancik M et al. NeRF: representing scenes as neural radiance fields for view synthesis. *Commun ACM* **65**, 99–106 (2021).

S4. Tancik M, Srinivasan PP, Mildenhall B et al. Fourier features let networks learn high frequency functions in low dimensional domains. In *Proceedings of the 34th International Conference on Neural Information Processing Systems* 632 (Curran Associates Inc, 2020). http://doi.org/10.5555/3495724.3496356.

S5. Tian L, Waller L. Quantitative differential phase contrast imaging in an led array microscope. *Opt Express* **23**, 11394–11403 (2015).

S6. Fan Y, Sun JS, Shu YF et al. Accurate quantitative phase imaging by differential phase contrast with partially coherent illumination: beyond weak object approximation. *Photonics Res* **11**, 442–455 (2023).

S7. Mehta SB, Sheppard CJ. Quantitative phase-gradient imaging at high resolution with asymmetric illumination-based differential phase contrast. *Opt Lett* **34**, 1924–1926 (2009).

S8. Zhang QR, Hu Q, Berlage C et al. Adaptive optics for optical microscopy [invited]. *Biomed Opt Express* **14**, 1732–1756 (2023).
S9. Lehtinen J, Munkberg J, Hasselgren J et al. Noise2noise: learning image restoration without clean data. In *Proceedings of the 35th International Conference on Machine Learning* 2965–2974 (PMLR, 2018).
S10. Bergeron RD, Burt PJ, Adelson EH. A multiresolution spline with application to image mosaics. *ACM Trans Graph* **2**, 217–236 (1983).
S11. Mittal A, Soundararajan R, Bovik AC. Making a "completely blind" image quality analyzer. *IEEE Signal Process Lett* **20**, 209–212 (2013).
S12. Eskicioglu AM, Fisher PS. Image quality measures and their performance. *IEEE Trans Commun* **43**, 2959–2965 (1995).
S13. Patterson MS, Foster FS. The improvement and quantitative assessment of b-mode images produced by an annular array/cone hybrid. *Ultrason Imaging* **5**, 195–213 (1983).
S14. Fan Y, Sun JS, Chen Q et al. Single-shot isotropic quantitative phase microscopy based on color-multiplexed differential phase contrast. *APL Photonics* **4**, 121301 (2019).